Efficient simulation of solution curves and bifurcation loci in injection-locked oscillators

Jesús de Cos and Almudena Suárez, *Fellow, IEEE*

***Abstract*—A new method is presented for the two-level harmonic-balance analysis of multivalued synchronized solution curves in injection-locked oscillators. The method is based on the extraction of a nonlinear admittance function, which describes the circuit response from the input source terminals. It does not require any optimization or parameter switching procedures, this constituting a significant advantage compared with previous analysis techniques. With additional mathematical conditions, it enables a straightforward determination of the turning point and Hopf bifurcation loci that delimit the stable injection-locked operation bands. The codimension two bifurcation point at which the turning point and Hopf bifurcation loci merge is analyzed in detail, as well as the saddle-connection locus. As it is shown, a second intersection of the saddle-connection locus with the turning point locus acts as a boundary between synchronization points and points associated with jumps and hysteresis. The likely observation of chaotic solutions in the neighborhood of the saddle-connection locus is discussed too. The techniques have been validated by application to several injection-locked oscillators, obtaining good agreement with the experimental results.**

***Index Terms*—Injection-locking, oscillator, harmonic balance (HB), bifurcation, stability.**

I. Introduction

Injection locking [1-3] has multiple applications, such as phase noise reduction [2-3], high-gain amplification [4-6], compact and low-cost phase and frequency modulation [7-9] and phase shifting [10-12]. Injection-locked oscillators exhibit solution curves with intricate geometries when traced versus the input frequency ω_s, injection current I_s and other parameters. For small input power, two different solution curves coexist [13-18]: a closed curve, composed of the actual injection-locked solutions, and a low-amplitude (non-oscillatory) open curve, defined for all frequency values. As the input power increases, both solution curves merge into a single one, exhibiting several turning points. Turning points (or infinite slope points) are thus intrinsic to the behavior of injection-locked oscillators. When approaching a turning point, convergence problems are typically found in default harmonic balance (HB) due to ill-conditioning of the Jacobian matrix. When occurring at low input power, turning points are associated with desynchronization: generation of a quasiperiodic solution at the two fundamentals ω_s and the autonomous frequency ω_a from zero frequency difference $\Omega = |\omega_s - \omega_a|$ [15-16,19-21]. For higher input power, the quasiperiodic solutions are typically generated at Hopf bifurcations, with frequency $\Omega = |\omega_s - \omega_a| \neq 0$ [13-14,19], and turning points of the periodic curves give rise to jump and hysteresis phenomena.

In previous works [14-16], auxiliary generators (AG) have been used to avoid undesired convergence to the low-amplitude non-oscillatory solution. The AG must fulfill a nonperturbation condition corresponding to the zero value of the AG current-to-voltage ratio ($Y_{AG} = 0$). The injection-locked solution curves, intrinsically exhibiting turning points, are obtained applying continuation methods (i.e. parameter switching) to the full HB system in in-house software [13-14], or to the AG outer tier system ($Y_{AG} = 0$) when using commercial HB software [22-24]. This outer tier is solved through optimization and the user is required to manually apply parameter switching, stopping each ill-convergence simulation and choosing a different analysis parameter. The procedure becomes cumbersome, especially in the region of intermediate input power.

Hopf bifurcation and turning point loci have a valuable practical interest since in the plane defined by the input power and input frequency (or other relevant parameters) the loci provide a "map" showing regions with different qualitative behavior, i.e. periodic, quasiperiodic and hysteresis [13-16]. In in-house software, tracing the bifurcation loci requires solving a mixed system of equations composed of the HB system and a bifurcation condition, based on the characteristic determinant [13-14], which depends on the perturbation frequency Ω. The frequency Ω should take zero value at turning points and be different from zero and incommensurable with ω_s at Hopf bifurcations. This procedure may have numerical difficulties associated with the significant variation in the order of magnitude of the characteristic determinant when modifying the analysis

Manuscript received February 24, 2014. This work was supported by the Spanish Ministry of Economy and Competitiveness under contract TEC2011-29264-C03-01 and the predoctoral fellowship for researchers in training of the University of Cantabria and the Regional Ministry of Education of the Government of Cantabria.

The authors are with the Communications Engineering Department, University of Cantabria, Escuela Técnica Superior de Ingenieros Industriales y de Telecomunicación (ETSIIT), 39005 Santander, Spain (e-mail: decosj@unican.es; suareza@unican.es).

parameters [19]. When using commercial HB, turning points are detected imposing the singularity of the 2×2 Jacobian matrix of the AG admittance function [25]. This requires fixing a proper threshold for the determinant value, compatible with the one fixed for the nonperturbation condition $Y_{AG}=0$. In turn, Hopf bifurcations are detected by means of an AG with amplitude tending to zero, operating at the frequency Ω and fulfilling the nonperturbation condition [15-16,19]. An additional problem comes from the fact that the turning point and Hopf bifurcation loci are often multivalued, this requiring the application of parameter switching [14,16,25-26].

A completely different procedure is proposed in this work, which, as presented, is valid for unilateral injection-locking, under the usual assumption of a perfectly sinusoidal synchronizing source. At a first stage, the injection source is suppressed and, instead, the AG is used to obtain an outer-tier admittance function Y_T describing the circuit response to an external excitation. This function will depend on the AG frequency ω and amplitude V. For each pair of values ω,V, the whole HB system (acting as an inner tier) is solved, with as many harmonic components as desired. At a second stage, and once $Y_T(\omega,V)$ has been determined, the injection-locked solution curve at the particular injection current I_s is directly obtained from the level curve of the surface $\Sigma(\omega,V)=|Y_T|V$ corresponding to I_s. High analysis sensitivity will be ensured by using the Norton equivalent of the input network seen from the analysis nodes. No optimization techniques are required. Once the surface Σ has been determined in a single initial simulation, solution curves for any input power or frequency values are directly calculated with no need to resimulate the circuit. In addition, the turning point locus is efficiently obtained with simple mathematical conditions, applied to the surface Σ. The Hopf bifurcation locus is calculated considering an additional dependence on the perturbation frequency ω_a. As shown in [16,19], turning points can correspond to either synchronization or jump phenomena. Another novelty of this paper is the investigation of the global bifurcation condition that distinguishes the two types of turning points.

The analysis methodology based on level curves is automatable and can be applied in combination with any standard HB software, without optimization tools or dedicated routines for bifurcation detection. Due to its computation efficiency, it can be used for an optimized design of injection-locked oscillators, globally accounting for their full response versus input power and frequency or other parameters. It is of general application to any nonlinear circuit and can be used for stability analysis and stabilization of power amplifiers, for instance [25-26]. Extensions of this method to the analysis of frequency dividers would be feasible although beyond the scope of this work. Here, it will be illustrated through its application to three injection-locked oscillators, enabling rigorous validations with the previous AG-based HB technique, time-domain methods and measurements. Note that the most accurate validation is with independent simulation techniques, as only in this case possible discrepancies should come from the method itself, instead of a deficient modeling of the nonlinear and linear elements.

The paper is organized as follows. Section II presents the new methodology to obtain the solution curves of an injection-locked oscillator. This procedure, as shown in Section III, enables direct calculation of the turning point locus and the synchronization bandwidth. Section IV presents a new technique for obtaining the Hopf bifurcation locus. Additional bifurcation points, responsible for chaotic behavior, are found in Section V with the aid of the Poincaré map. Section VI presents the application of the methodology to the experimental oscillator at 12.7 GHz.

II. Outer-tier contour

Any injection-locked oscillator can be represented as the parallel connection of an oscillator block (with arbitrary complexity) and the Norton equivalent of the input source, assumed to be sinusoidal. The simplified equivalent circuit is depicted in Fig. 1(a). The oscillator block will be described with an admittance function. Note that a series representation, in terms of an impedance function, is also possible [16] and will be better suited in the case of reduced controllability and/or observability [27-28] with the parallel excitation.

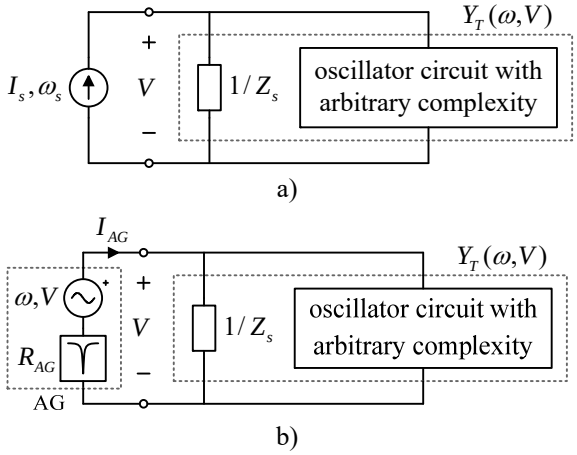

Fig. 1. (a) One-port representation of an injection-locked oscillator using an admittance description. (b) After suppressing the injection source, a voltage auxiliary generator is connected in parallel to obtain the nonlinear admittance model of the oscillator.

A. Periodic solution curves

To obtain the admittance description of the oscillator block, the injection source will be suppressed and a voltage AG will be introduced into the circuit instead (Fig. 1). In most cases, this AG can be directly connected to the nodes where the injection source was at [see Fig. 1(b)]. Exceptions, requiring the Norton equivalent, are considered later in this section. The AG will constitute an excitation source, used to obtain a

nonlinear admittance model of the whole oscillator circuit. The model will depend on the AG frequency ω and amplitude V. To obtain the admittance function $Y_T(\omega,V)$, a double sweep is performed in ω and V. The frequency interval should comprise the one through which the oscillator will be injected with the independent source and include the free-running frequency or frequencies, estimated from an initial stability analysis of the circuit dc solution. In turn, the amplitude interval can be estimated from the ratings of the transistor. For each pair of values ω,V, a whole HB resolution of the AG-excited circuit, operating in forced manner, is carried out, with as many harmonic terms as necessary. This can be formulated as:

$$\begin{aligned} &\bar{H}(\bar{X},\omega,V)=0 \\ &Y_T(\omega,V)=I_{AG}[1]/V \end{aligned} \tag{1}$$

where $\bar{H}$ is the HB error function, $\bar{X}$ are the Fourier coefficients of the node voltages and inductor currents and $I_{AG}[1]$ represents the first harmonic of the AG current. The first equation corresponds to the harmonic balance system, with NH harmonic components. Indeed, the AG operates as an independent periodic generator connected to the circuit, as explicitly shown in (1)(a). Remember that the injection source is suppressed while obtaining the admittance model [Fig. 1(b)]. The admittance function in (1)(b) is calculated from the ratio between the current through the AG (entering the circuit) and the excitation voltage.

In a second stage, the injection source I_s is considered. The current-type injection source operates at the fundamental frequency ω_s and constitutes an open circuit at all the harmonic terms $k\omega_s$ with $k\neq 1$. Applying Kirchhoff's current law to the circuit in Fig. 1(a), the following equation can be formulated:

$$Y_T(\omega,V)V-I_s e^{j\phi}=0 \tag{2}$$

where I_s and ϕ are respectively the injection current level and the phase shift between the input source and the first harmonic of the voltage across its terminals. Squaring and adding the real and imaginary parts of (2):

$$\left|Y_T(\omega,V)\right|^2 V^2-I_s^2=0 \tag{3}$$

Note that the three squared quantities in (3) are always positive, so the square root can be taken to finally obtain:

$$I_s=\left|Y_T(\omega,V)\right|V \tag{4}$$

The phase shift ϕ can be calculated from the real and imaginary parts of (2):

$$\phi=\arg\left[Y_T(\omega,V)\right] \tag{5}$$

The scalar current equation (4) describes a surface on the plane ω,V and, as shown in the following, can provide the injection-locked periodic solution curves with an accuracy equivalent to a full HB analysis of the injection-locked oscillator. Let the function

$$\Sigma(\omega,V)=\left|Y_T(\omega,V)\right|V \tag{6}$$

be considered. The periodic solution curves can be obtained from the intersections of the surface (6) with horizontal planes for different values of injection current (Fig. 2). This constitutes the contour plot of (6). For a proper computation of the surface, it is convenient to first perform a coarse sweep. If the curves are not smooth or regular, a finer sweep should be used. The easiest is to use linear sweeps, just to obtain homogeneous data for computing the results.

The level curve of the differentiable function $\Sigma:\mathbb{R}^2\rightarrow\mathbb{R}^+$ corresponding to a real positive value I_s is the set of points

$$\left\{(\omega_s,V_s)\in\mathbb{R}^2:\Sigma(\omega_s,V_s)=I_s\right\} \tag{7}$$

The graphical representation of a set of level curves is the contour plot of the surface Σ. The intersections (7) can be obtained with external software although commercial HB simulators usually provide the user with a function that computes the contour plot. The accuracy of the solutions obtained is generally excellent assuming the frequency and voltage steps used in the double sweep are properly chosen. As shown in Fig. 2, turning points of the solution curves are directly obtained with this method without any optimization or parameter switching procedures.

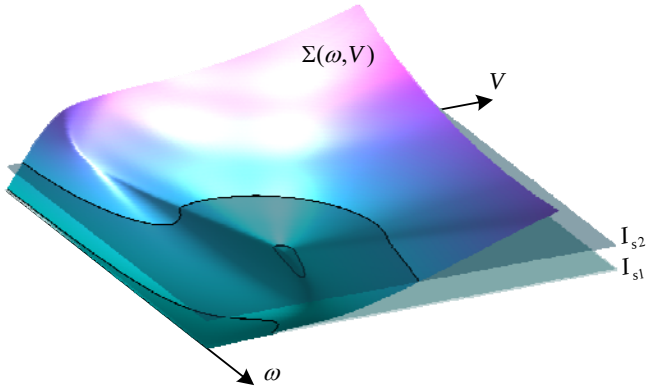

Fig. 2. Graphical illustration of the outer-tier contour, applied to obtain the solution curves of an injection-locked oscillator. As an example, two sets of curves, corresponding to different qualitative behavior of the oscillator, are obtained by means of the intersections of the secant planes I_{s1} and I_{s2} with the surface Σ. These current values correspond to input power values −20 dBm and 0 dBm, respectively. The data are obtained from the circuit in Fig. 4(a), later analyzed.

B. Application examples

For illustration, the above methodology has been applied to two oscillators with different topologies: a ring oscillator and a feedback LC oscillator. The first oscillator analyzed [Fig. 3(a)] is a single-ended three-stage ring oscillator at 2.5 GHz with transistors described by Angelov's FET model [29] and RC loads. Initially, no parasitic elements in the transistor

model are considered, so, in time domain, the circuit is governed by a three-dimensional system. This will enable a detailed analysis of its nonlinear dynamics by means of the Poincaré map (Section V-B), which in the case of a system of three dimensions admits a planar representation. A realistic description of the transistor, including all the parasitics, is considered in Section VI, where measurements are also presented.

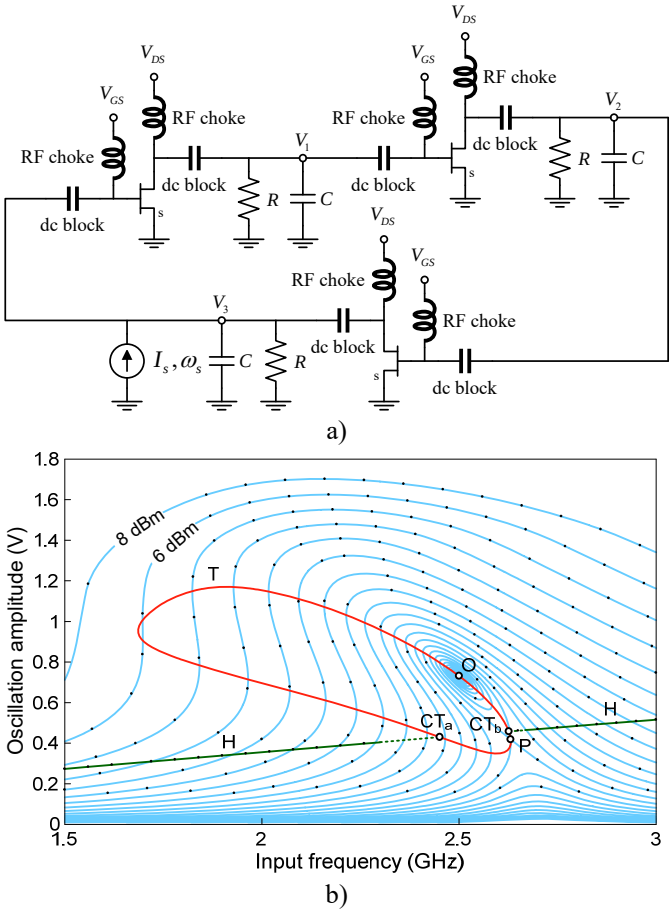

Fig. 3. (a) Single-ended three-stage ring oscillator with transistors described by Angelov's FET model with no parasitic elements (admitting a planar representation of the Poincaré map) and RC loads. (b) Periodic solution curves versus input frequency for different values of input power (isolines with 2 dB step) and bifurcation loci, obtained with the new methodologies described in Sections II, III, IV. The results (solid lines) are compared with those obtained with standard AG optimization and parameter switching [16] (dots). In all cases the HB system has been solved using $NH = 15$ harmonic terms.

The periodic solution curves obtained applying the outer-tier contour to the circuit in Fig. 3(a) are shown in Fig. 3(b), fully matching the results obtained with standard optimization and parameter switching, also included in the figure. The new analysis based on the level curve computation is straightforward, with no need of optimization or complex techniques such as parameter switching to pass through the turning points intrinsic to the injection-locked operation. For a rigorous comparison, the same number of harmonic terms $NH = 15$ have been considered in standard optimization with parameter switching. Both methods show excellent agreement.

Note that no approximation has been performed when developing the formulation (4), so the equation predicts exact circuit solutions, up to the HB analysis error. Assuming the double sweep intervals are large enough, equation (4) allows predicting every coexisting periodic solution without missing any, as for each frequency value ω every amplitude value V is covered in the double sweep. A relevant aspect of (4) is that there is no explicit dependence on the phase of the input source, thus providing an interesting result: the periodic solution curves from an injection-locked oscillator can actually be computed from data collected in the absence of the input source. This is why the AG phase can be arbitrarily set to any value, zero for instance. Emphasis should be made on the fact that the method presented is not a describing-function approach [30]. On the contrary, $NH = 15$ harmonic terms are considered in the calculation of the outer-tier admittance function $Y_T(\omega, V)$ in all examples shown in this work. Furthermore, this particular number of harmonic terms enables maximizing the computational efficiency when solving the HB system using Krylov subspaces [31-32], as the computational complexity depends on the size of the FFT [33].

The outer-tier contour method is automatable and easily combinable with any HB simulator, either in-house or commercial. It is highly advantageous, not only for a reduction of the simulation time, which is significant as no optimization is used, but also for the fact that no parameter switching is needed; in simulations based on commercial HB, the user has to take decisions on which parameter to sweep in view of the geometry of the curves. As shown in next sections, the method allows an equally efficient determination of the bifurcation loci.

The second circuit analyzed with the outer-tier contour [Fig. 4(a)] is a feedback LC oscillator at 2.5 GHz, using a NE3210S01 FET in common gate. The objective is to perform an exhaustive comparison of the outer-tier contour method technique with time-domain integration. Unlike the previous case, the complete transistor model, including parasitics, has been considered. In turn, the linear elements are assumed ideal to avoid descriptions based on scattering parameters by the manufacturers. The results obtained with the new method are compared in Fig. 4(b) with those obtained with full HB and AG optimization combined with parameter switching. Both methods show excellent agreement. Next, a comparison with time-domain analysis has been carried out. The input frequency ω_s has been swept at a constant input power of −10 dBm. Fig. 5(a) shows the bifurcation diagram obtained in time domain. At each input frequency value, the steady-state solution is sampled at multiples of the input signal period $T = 2\pi/\omega_s$. In this manner, a single point is obtained if the period of the solution agrees with T (synchronized regime) and a distribution of multiple points if the solution is unlocked. The synchronization bandwidth [Fig. 5(a)] shows a very good agreement with the one predicted by the new method. After each time-domain simulation, the magnitude of the first harmonic of the node voltage has also been calculated

from the spectrum of the steady-state solution. The variation of this magnitude versus the input frequency ω_s is traced in Fig. 5(b), where it can be compared with the corresponding isoline obtained with the outer-tier contour method. The stable section of the solution curve is delimited by the points T_1 (synchronization turning point) and H_1 (Hopf bifurcation). The agreement is excellent. Similar comparisons have also been exhaustively carried out for other input power values.

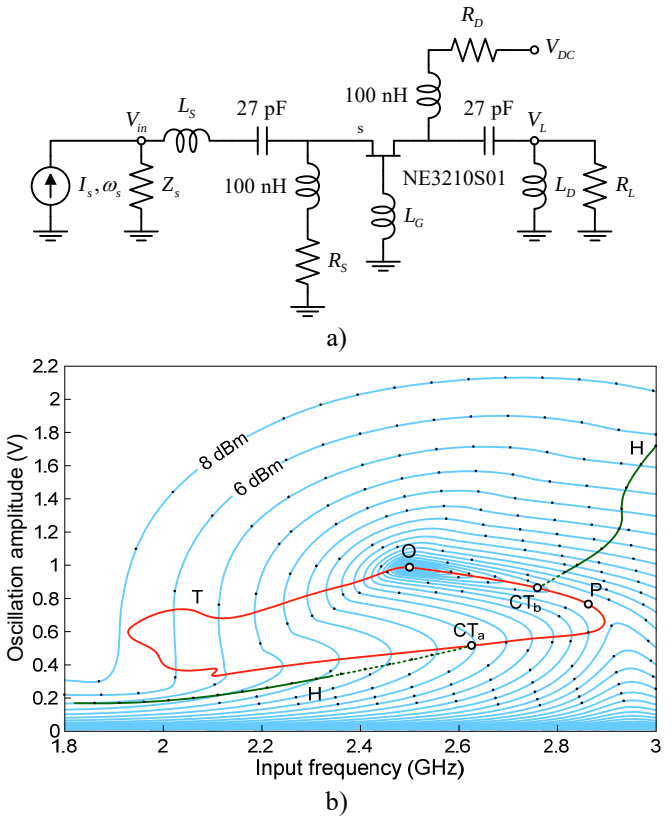

Fig. 4. (a) Feedback LC oscillator based on NE3210S01 FET in common gate. (b) Periodic solution curves versus input frequency for different values of input power (isolines with 2 dB step) and bifurcation loci, obtained with the new methodologies described in Sections II, III, IV. The results (solid lines) are compared with those obtained with standard AG optimization and parameter switching [16] (dots). In all cases the HB system has been solved using $NH = 15$ harmonic terms.

Tables I and II present a comparison of the computational effort of the new method (outer-tier contour) and the previous method based on AG optimization to fulfill $Y_{AG} = 0$, plus parameter switching. Table I corresponds to the ring oscillator in Fig. 3(a) and shows a speedup of 5.25. Table II corresponds to the LC oscillator in Fig. 4(a) and shows a speedup of 2.3. In the case of the existing AG method, the numbers correspond exclusively to active simulation time. The time devoted to inspect the curves, take decisions on which parameter to sweep and apply manually parameter switching is not included. In the case of the new method, the time is devoted to the double sweep used in the outer-tier contour. The time required to compute the data from the double sweep is negligible. One significant advantage of the new method is that once the outer-tier contour has been obtained, one can trace as many solution curves as desired, in the frequency and amplitude intervals covered by the double sweep. On the contrary, the existing methods can only provide a finite set of solution curves for particular values of input power, as these curves should be obtained one by one.

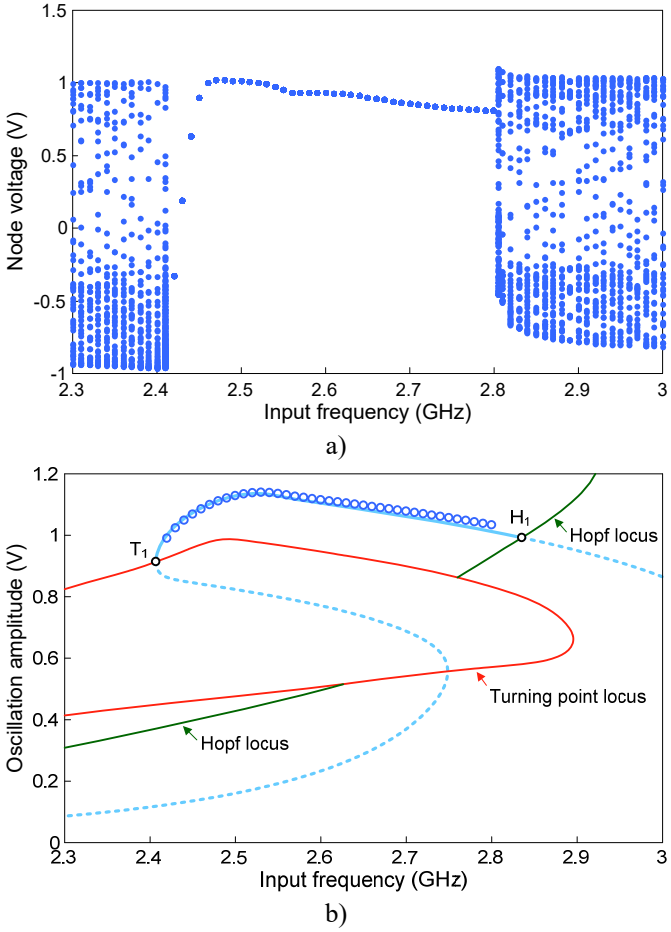

Fig. 5. Comparison of the outer-tier contour method with time-domain integration for an input power value of −10 dBm. (a) Bifurcation diagram obtained in time domain. The steady-state solution is sampled at integer multiples of the input generator period T. (b) Magnitude of the first harmonic from the spectra of the solutions obtained with time-domain integration (dots) and the corresponding isoline obtained with the outer tier contour. The stable section is delimited by the points T_1 (synchronization turning point) and H_1 (Hopf bifurcation).

TABLE I
COMPUTATIONAL EFFORT DEVOTED TO THE CIRCUIT IN FIG. 3(A).

	Number of simulations	Simulation time (minutes)	Number of solution curves
Existing method	38029	43.1	25
New method	51471	8.2	∞

TABLE II
COMPUTATIONAL EFFORT DEVOTED TO THE CIRCUIT IN FIG. 4(A).

	Number of simulations	Simulation time (minutes)	Number of solution curves
Existing method	39923	39.52	32
New method	103389	17.2	∞

C. Generalization

In some oscillator circuits one problem can arise: the observation nodes where the input source is connected may not be sensitive enough to excite all the coexisting solutions. This can be circumvented by choosing the sensitive nodes and calculating the Norton equivalent of the input network seen from that nodes [13]. The sensitive nodes usually correspond to the active device terminals, since the active devices constitute the "sources" of negative resistance existing in the circuit. In the generalized method, the input source will be connected to the internal nodes by means of a linear network of arbitrary complexity, possibly including transmission lines. It is therefore plausible to represent this last one as a two-port network described with scattering parameters. Fig. 6(a) sketches this scenario. The Norton equivalent is applied to the fundamental frequency ω_s, as shown in Fig. 6(b). The setup in Fig. 6(c) allows for properly obtaining Y_i. The input source is suppressed and an ideal high pass filter is included between the internal nodes and the input network. The purpose of this filter is to prevent the influence of the input network at the fundamental frequency, so that that the Norton equivalent can be used instead. The cutoff frequency of the ideal filter can be arbitrarily set between the first and second harmonic. From Fig. 6(a), the Norton equivalent current at the internal nodes is:

$$I_N = \frac{2S_{21}}{1-S_{11}-(\Delta-S_{22})} I_s \tag{8}$$

where $\Delta = S_{11}S_{22} - S_{12}S_{21}$. The Norton equivalent impedance is

$$Z_N = Z_0 \frac{1-S_{11}-(\Delta-S_{22})}{1-S_{11}+(\Delta-S_{22})} \tag{9}$$

where Z_0 is the characteristic impedance. The equivalent circuit is represented in Fig. 6(b), which is analogous to the circuit in Fig. 1(a), so the formulation developed applies identically. The Norton current is frequency-dependant but it is directly proportional to the injection current I_s. Applying (2) to the circuit in Fig. 6(b):

$$\left[1/Z_N(\omega) + Y_i(\omega,V_i)\right]V_i - I_N(\omega)e^{j\phi_i} = 0 \tag{10}$$

where Y_i is the internal admittance function of the oscillator seen from the internal nodes, V_i is the voltage amplitude of the first harmonic and ϕ_i is the phase shift between the Norton equivalent current and the first harmonic of the voltage across the internal terminals. Substituting (8), (9) in (10) and reordering terms:

$$\frac{Y_0\left[1-S_{11}+(\Delta-S_{22})\right]+Y_i\left[1-S_{11}-(\Delta-S_{22})\right]}{2S_{21}} V_i = I_s e^{j\phi_i} \tag{11}$$

where $Y_0 = 1/Z_0$ is the characteristic admittance. Again, squaring and adding the real and imaginary parts of (11) and taking the square root of both sides:

$$I_s = \frac{\left|Y_0\left[1-S_{11}+(\Delta-S_{22})\right]+Y_i\left[1-S_{11}-(\Delta-S_{22})\right]\right|}{2\left|S_{21}\right|} V_i \tag{12}$$

Note that (12) is in fact (4) evaluated at the internal nodes. The phase shift ϕ_i is calculated from the real and imaginary parts of (11):

$$\phi_i = \arg\left[\frac{Y_0\left[1-S_{11}+(\Delta-S_{22})\right]+Y_i\left[1-S_{11}-(\Delta-S_{22})\right]}{2S_{21}}\right] \tag{13}$$

From (12), the solution curves of an injection-locked oscillator can be computed combining the results of two independent simulations: an S-parameter simulation of the linear network between the input source and the sensitive internal nodes [Fig. 6(a)], and a double sweep in HB to obtain the internal admittance function $Y_i(\omega,V_i)$. Note that the frequency points of both sweeps should agree for computational convenience.

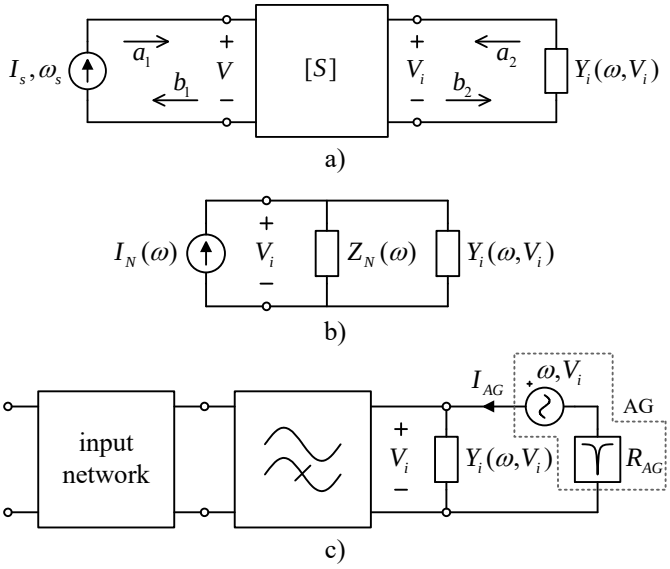

Fig. 6. (a) A suitable observation nodes for applying the outer-tier contour to an oscillator may be connected to the input source by means of a linear network described with scattering parameters. (b) Norton equivalent of the input circuit. (c) A suitable setup for properly obtaining the nonlinear internal admittance function.

Solution curves can be traced in terms of any state variable. To do this, (13) is interpolated at the values of input frequency and internal voltage amplitude of the first harmonic computed with the contour of (12). Note that to refer the phase shift value to the internal nodes, the opposite sign of (13) should be considered. Then, the values of injection current, input frequency, internal voltage amplitude and phase shift are exported to the HB simulator. These values are respectively provided to the input source and to an AG connected to the internal nodes. No optimization is required as the solutions

have already been calculated with the outer-tier contour. The solution curves in terms of the desired state variable are finally obtained through an ordinary HB simulation.

The generalized outer-tier contour method has been applied to an experimental ring oscillator that will be analyzed in detail in Section VI.

III. Turning Point Locus

The turning point locus is the set of points of the solution curves satisfying infinite slope, which generally corresponds to a closed curve [14-18]. A mathematical condition for this locus, relying on the use of an AG, is given in [15-16,19] and corresponds to the singularity of the Jacobian matrix of the AG admittance function Y_{AG}. Using this condition in combination with commercial HB is demanding since it requires a calculation of the AG derivatives through finite differences [23], as well as the choice of a convenient threshold for the determinant of the Jacobian matrix. The formulation based on (4) offers a new methodology for the calculation of the turning point locus, compatible with the use of commercial HB software. In fact, the turning point locus is the set of points of the surface (6) satisfying zero partial derivative with respect to V. It is convenient to compute first the numerical gradient of (6) for later use:

$$\nabla\Sigma = \begin{bmatrix} \partial\Sigma/\partial\omega \\ \partial\Sigma/\partial V \end{bmatrix} \tag{14}$$

Then, the turning point locus is given by the zero-level contour of the V component of (14):

$$T = \left\{ (\omega_s, V_s) \in \mathbb{R}^2 : \frac{\partial\Sigma}{\partial V}(\omega_s, V_s) = 0 \right\} \tag{15}$$

Expression (15) has been applied to the two oscillators previously considered, providing the results in Figs. 3(b), 4(b). The accuracy of the method is excellent since the turning point locus obtained intersects the solution curves at the infinite slope points. However, the practical interest of the turning point locus is evidenced by its representation in the plane defined by the input frequency ω_s and injection current I_s. In this plane, the turning point and Hopf bifurcation loci provide a "map" showing regions with different qualitative behavior. Obtaining the turning point locus in the plane (ω_s, I_s) is only possible with a dedicated solution of the circuit, including the singularity condition. Indeed, the parameters (ω_s, I_s) can be calculated through interpolation of (4) at the locus points (ω_s, V_s) obtained with (15). Fig. 7 presents the turning point locus in the plane (ω_s, I_s), corresponding to the circuits in Fig. 3(a) and Fig. 4(a). The Hopf bifurcation locus has also been included, which will be analyzed in Section IV.

The turning point locus in the plane (ω_s, I_s) has a curvilinear-triangle shape, divided in two sections by the points CT_a and CT_b. Through the turning point locus, a real pole stays at zero. In the section $CT_a - O - CT_b$, exhibiting a V shape, all the rest of system poles are on the left-hand side of the complex plane (LHP). The turning points in this section correspond to either synchronization or jumps (the latter occurring in hysteresis cycles). The global bifurcation [20] that distinguishes the two types of points is analyzed in Section V. The remaining section of the turning point locus $CT_a - P - CT_b$ has a real pole on the right-hand side of the complex plane (RHP) (besides the real pole on the imaginary axis). Due to the presence of this unstable pole, the crossing of section $CT_a - P - CT_b$ has no physical impact.

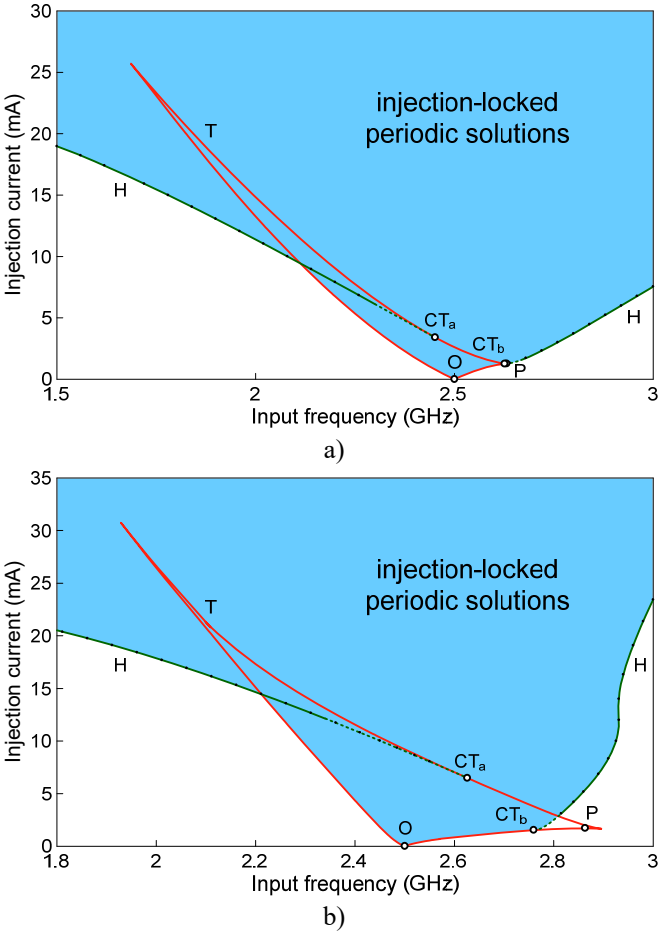

Fig. 7. Turning point and Hopf bifurcation loci represented in the plane defined by the input frequency and injection current. The Hopf bifurcation points obtained with the technique described in Section IV (solid lines) are contrasted with those obtained with standard optimization (dots). The codimension two bifurcations are also included, obtained by extrapolation of the Hopf bifurcation locus. (a) Single-ended three-stage ring oscillator with transistors described by Angelov's FET model with no parasitic elements and RC loads. (b) Feedback LC oscillator based on NE3210S01 FET in common gate.

A. *Free-running solution and merging point*

For very low input power, a perfect ellipse coexists with a low-amplitude open curve. Note that for zero input power, the ellipse degenerates into a point corresponding to the free-running solution and the open curve becomes the horizontal axis $V_s = 0$, corresponding to the unstable dc solution that

coexists with the free-running oscillation. As the input power increases, the perfect ellipse gets progressively distorted and, for a particular input power value, this closed curve merges with the low-amplitude solution providing a single open curve. So on, for convenience, the point at which both curves merge will be referred to as "*merging point*".

The free-running solution and merging points can be easily computed from the surface (6). Remember that I_s can only take positive real values. The free-running solution O is the minimum of the surface at (ω_o, V_o), where Σ takes zero value. The point O is therefore a stationary point of Σ and satisfies zero value of the gradient (14). The free-running solution is computed as the intersection of the zero-level contours of the ω and V components of $\nabla\Sigma$ for $I_s = 0$:

$$O = \left\{(\omega_s, V_s) \in \mathbb{R}^2 : \frac{\partial \Sigma}{\partial V}(\omega_s, V_s) = 0\right\} \bigcap \left\{(\omega_s, V_s) \in \mathbb{R}^2 : \frac{\partial \Sigma}{\partial \omega}(\omega_s, V_s) = 0\right\} \quad \text{with} \quad I_s = 0 \tag{16}$$

The merging point P of the solution curves is a saddle point of Σ and will satisfy zero gradient. A geometrical saddle point of a surface (not to confuse with saddle-type equilibria) is a stationary point but not an extremum [34]. At the saddle point, the contour plot of the surface appears to intersect itself, that is, the contour lines merge at the saddle point. The merging point is computed as the intersection of the zero-level contours of the ω and V components of $\nabla\Sigma$ for $I_s \neq 0$:

$$P = \left\{(\omega_s, V_s) \in \mathbb{R}^2 : \frac{\partial \Sigma}{\partial V}(\omega_s, V_s) = 0\right\} \bigcap \left\{(\omega_s, V_s) \in \mathbb{R}^2 : \frac{\partial \Sigma}{\partial \omega}(\omega_s, V_s) = 0\right\} \quad \text{with} \quad I_s \neq 0 \tag{17}$$

Expressions (16) and (17) have been applied to the two oscillators under study. The results are shown in Figs. 3(b), 4(b) and directly provide the free-running and merging point solutions, respectively denoted as O and P. The solutions O and P have also been represented in the plane (ω_s, I_s) of Fig. 7, obtained by interpolation of equation (4) at the points (ω_s, V_s) given by (16) and (17), respectively.

B. Synchronization bandwidth and region of linear operation

From zero input power up to that corresponding to P, the synchronization bandwidth is delimited by two turning points of the closed curve, one at each side. For higher input power, Hopf bifurcations will arise in the system and will also be responsible for the oscillator unlocking. Up to the point P, the turning points are in fact *local-global bifurcations* [21,35-36] or synchronization points. Therefore, the synchronization bandwidth for a particular injection current value I_s is directly given by the frequency difference of the corresponding two points of the $CT_a - O - CT_b$ section of the turning points locus (15) when represented in the plane (ω_s, I_s). The synchronization bandwidths of the oscillators in Figs. 3(a), 4(a) have been represented versus input power in the plots on the left side of Fig. 8.

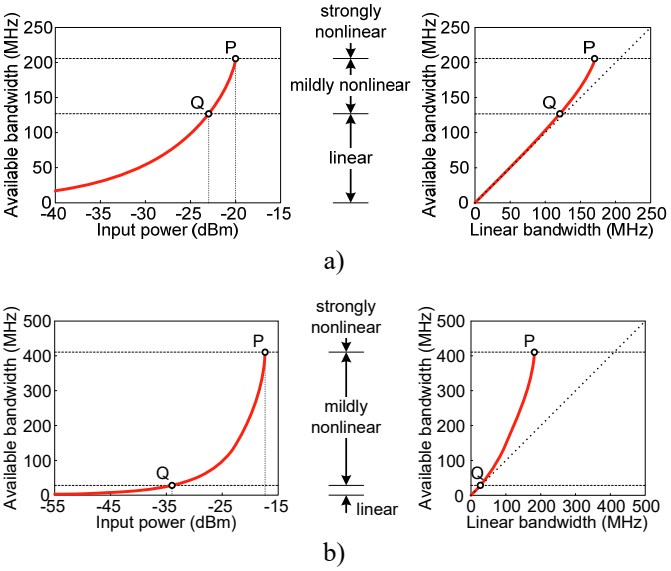

Fig. 8. Maximum available synchronization bandwidth. The 5% expansion point (Q) and merging point (P) have been included to delimit the regions of operation. (a) Single-ended three-stage ring oscillator with transistors described by Angelov's FET model with no parasitic elements and RC loads. (b) Feedback LC oscillator based on NE3210S01 FET in common gate.

The new method will be compared with previous models valid for low injection current [22-23]. Under low injection current, it is possible to linearize the admittance function describing the oscillator response about the free-running solution. The linearized model is written in terms of the partial derivatives of the admittance function, calculated by application of finite differences to the same AG used to obtain the circuit free-running oscillation [22-23]. This model predicts linear synchronization bandwidth versus the injection current I_s:

$$\Delta\omega_{\max}(I_s) = \frac{2\left|Y_{ToV}\right|}{V_o\left(Y_{ToV} \times Y_{To\omega}\right)} I_s \tag{18}$$

where $Y_{ToV}, Y_{To\omega}$ are the partial derivatives of the total admittance with respect to the voltage and frequency, respectively, calculated about the free-running point (ω_o, V_o), V_o is the oscillation amplitude and the product is $a \times b = a^r b^i - a^i b^r = |a||b|\sin\left[\arg(b) - \arg(a)\right]$.

The bandwidth obtained with the new method has been compared with the one predicted with the linearized model given in (18) when increasing the input power. As expected, for low input power there is very good agreement. However, when the injection-locked oscillator enters the nonlinear regime the actual bandwidth deviates from the one predicted with (18), either compressing or expanding with respect to this

linear behavior. There are examples of both expansion [37] and compression [38] in the literature. A figure of merit can be defined for the linearity of injection-locked oscillators, for instance, the input power corresponding to 5% compression/expansion of the linear bandwidth. The 5% compression/expansion point, denoted Q in the diagrams of Fig. 8, can be considered to be the limit of linear operation with respect to the input source. The actual maximum available bandwidth, calculated with the new methodology, has been represented versus the linear bandwidth calculated with (18) on the right side of Fig. 8 for the two different oscillators considered so far. Interestingly, both oscillators expand their synchronization bandwidths as they progressively enter the nonlinear operation region. The merging point P have been also included in Fig. 8.

To summarize, from input power arbitrarily low up to the 5% compression/expansion point, the oscillator will operate mostly linearly with respect to the input source. From the 5% compression/expansion point up to the merging point, the oscillator will operate mildly nonlinearly. From the merging point, the oscillator will operate strongly nonlinearly. The three regions have been delimited in Fig. 8.

The new method presented for the calculation of the synchronization bandwidth is extremely powerful. The maximum available synchronization bandwidth is directly calculated with the contour computation in a manner similar to the injection-locked solution curves and the turning point locus. The method is equally accurate and effective, as well automatable and easily combinable with any HB simulator, either in-house or commercial. It must be noted that everything is obtained from just a single HB simulation in which the double frequency-amplitude sweep is performed.

IV. HOPF BIFURCATION LOCUS

At a Hopf bifurcation from periodic regime, a pair of complex-conjugate poles $\sigma \pm j\Omega$ crosses the imaginary axis to the RHP [13-14,39-40], which gives rise to a quasiperiodic solution at ω_s and Ω, with $\Omega = |\omega_s - \omega_a|$. The Hopf bifurcation locus is an open curve in the plane ω_s, V_s composed of all the points where Hopf bifurcations occur [13-14]. In fact, Hopf bifurcations delimit the stable synchronization ranges for intermediate input power level and high input power level, and generally occur in the low amplitude sections of the periodic solution curves. These low-amplitude sections of the periodic solutions can be obtained with a default HB simulation, excited with the actual synchronization source, instead of the auxiliary generator. Taking this into account, the new method, the zero-level contour technique, is based on the calculation of an admittance function describing the circuit response to the unknown perturbation frequency.

At a Hopf bifurcation, the oscillation amplitude at the incommensurable frequency ω_a tends to zero. Taking ω_s, I_s as parameters, the Hopf locus can be obtained [15-16,19] introducing a small-signal current source at ω_a into the circuit, which must fulfill:

$$Y_a(\omega_s, I_s, \omega_a) = 0 \tag{19}$$

To trace the Hopf bifurcation locus, the frequency ω_s is swept, solving (19) for I_s and ω_a at each sweep step. However, in the case of a multivalued locus, parameter switching must be applied. An alternative method is proposed here. For each input frequency ω_s, a relatively fine sweep is carried out in I_s. At each I_s step, a HB analysis is performed (with as many harmonic terms as desired), followed by a conversion-matrix sweep [41-42] in the perturbation frequency ω_a. The above procedure provides the perturbation admittance function $Y_a(\omega_s, I_s, \omega_a)$. Then, the Hopf bifurcation locus is computed for each value ω_s as the intersection of the zero-level contours of the real and imaginary parts of Y_a:

$$\begin{aligned} H(\omega_s) = &\left\{(I_s, \omega_a) \in \mathbb{R}^2 : \mathrm{Re}\left[Y_a(\omega_s, I_s, \omega_a)\right] = 0\right\} \\ &\bigcap \left\{(I_s, \omega_a) \in \mathbb{R}^2 : \mathrm{Im}\left[Y_a(\omega_s, I_s, \omega_a)\right] = 0\right\} \end{aligned} \tag{20}$$

Expression (20) provides the pairs of values (I_s, ω_a) corresponding to all the Hopf bifurcation points obtained for ω_s. The new method is, in general, computationally more expensive than the one based on (19) in the case of regular (single-valued) behavior of the Hopf bifurcation locus. However, if it is multivalued, which is not unusual in microwave circuits, the new method offers superior capabilities, since it enables a global exploration of the parameter space in search for Hopf bifurcations. An example of Hopf bifurcation locus that could not be traced with the existing method [based on solving (19)] will be presented in Section VI.

The method (20) has been applied to the oscillators in Figs. 3(a), 4(a), with the results included in Figs. 3(b), 4(b). Fig. 7 shows the turning point and Hopf bifurcation loci represented in the plane (ω_s, I_s). The circuit behaves in periodic regime in the shaded region. Outside this region the circuit response is quasiperiodic at the fundamental frequencies ω_s and Ω, where $\Omega = |\omega_s - \omega_a|$.

As will be discussed in Section V, the Hopf bifurcation locus merges tangentially with the turning point locus at the points CT_a and CT_b. As a result, the complex admittance surface Y_a folds at these two points and is multivalued in their neighborhoods. This gives rise to severe numerical problems that equally affect the standard optimization and the zero-level contour technique. However, with the latter, the advantage is the complex surface Y_a is available to diagnose conflictive points. On the other hand, the Hopf bifurcation locus is not expected to vary significantly in this region and will just merge tangentially with the turning point locus. Therefore, extrapolation of the Hopf bifurcation points already calculated

can be applied to obtain the remaining ones and the intersections CT_a and CT_b. These extrapolated points are shown in dashed line in the results of Figs. 3(b), 4(b), 7.

V. Additional Bifurcation Points

The Hopf bifurcation and turning point loci meet at two different points CT_a and CT_b. These points are codimension two bifurcations, this meaning that two parameters must be simultaneously varied to obtain the bifurcation point [20-21,43]. Indeed, the imaginary part of the critical pair of complex-conjugate poles involved in the Hopf bifurcation decreases when moving towards the codimension two bifurcation. It becomes zero at the codimension two bifurcation, where the two complex-conjugate poles turn into two real poles of zero value. This is why this bifurcation is known as double-zero eigenvalue. The real pole on the RHP in section $CT_a - P - CT_b$ passes through zero at each codimension two bifurcation (CT_a and CT_b).

A. Global bifurcations

As already stated, the points within the physical section of the turning point locus ($CT_a - O - CT_b$) can give rise to two different phenomena: synchronization or jumps. For low input power, these points will be synchronization points as this is the only possible transition mechanism from quasiperiodic to periodic regime (or vice versa). For higher input power, the Hopf bifurcation locus is traversed and at each Hopf bifurcation a quasiperiodic (unlocked) solution is necessarily generated. In these conditions, turning points are expected to correspond to jump points. Now, consider the bifurcation diagram shown in Fig. 9. Solely with the above consideration in mind, it is not possible to discern the behavior of the turning points in the section $T_\alpha - T_\beta$. The point T_x is taken for illustration. When crossing T_x for constant injection current, the Hopf bifurcation locus is not traversed, as indicated in Fig. 9. T_x should be a synchronization point. However, when crossing T_x for constant input frequency, the Hopf bifurcation locus is actually traversed, as indicated in the figure, which suggests T_x is a jump point. The nature of the turning points (synchronization or jump) cannot change depending on the parameter varied. Therefore, T_x corresponds to a synchronization point. A question arises then regarding the evolution of the quasiperiodic solution that is necessarily generated at the Hopf bifurcation H_1 in Fig. 9.

The solution curves obtained for constant injection current $I_s = 1.772$ mA and constant input frequency $f_s = 2.4$ GHz, passing through T_x, are explicitly shown in Fig. 10(a) and Fig. 10(b), respectively. The stability along the curves is indicated in the insets, as verified with pole-zero identification [44]. The nature of T_x is evidenced in Fig. 10(a): T_x is a synchronization point since it is the only periodic point where the quasiperiodic regime can be extinguished. This is because the Hopf bifurcation locus is never traversed for the constant current $I_s = 1.772$ mA. T_x is therefore a synchronization point also in Fig. 10(b). Solutions in between $T_x - T_1$ in Fig. 10(a) are of saddle type [20,45]. In analogous manner, solutions in between $T_x - T_2$ in Fig. 10(b) are also of saddle type. The periodic solution curve in Fig. 10(b) becomes stable at T_2 and remains stable up to the Hopf bifurcation H_1, where a quasiperiodic solution is generated. This quasiperiodic regime should be extinguished in an additional bifurcation. As will be shown, the fact that solutions in between $T_x - T_2$ are of saddle type is the key to understand the system behavior in the uncertainty region $T_\alpha - T_\beta$.

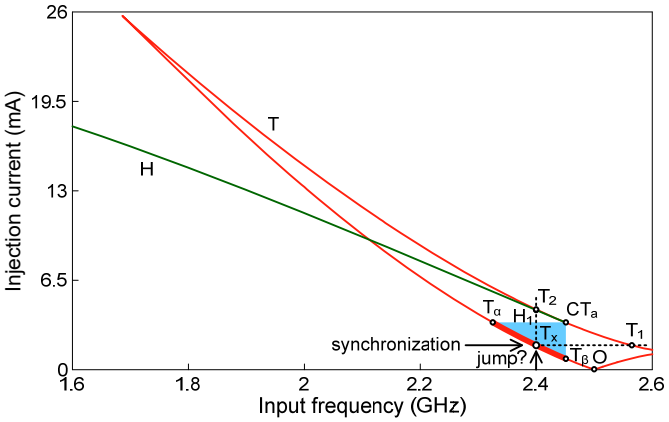

Fig. 9. The section $T_\alpha - T_\beta$ of the turning point locus of Fig. 7(a) shows ambiguous behavior. Consider the point T_x for instance: it is a synchronization point because no intersection with the Hopf bifurcation locus is observed when crossing T_x for constant injection current. However, the Hopf bifurcation locus is actually crossed from T_x when increasing the injection current for constant input frequency. This fact suggests it is a jump point, so additional bifurcation points should clarify the situation.

The existence of additional bifurcation points (different from turning points or Hopf bifurcations) was conjectured by Cartwright [20] on the study of Van der Pol's equation. These bifurcation points are in fact global bifurcations and are studied in the phase space [20,45]. Indeed, global bifurcations involve the interaction of several solutions in a subset of the phase space [20,45-46] and cannot be detected using local stability analyses. The study was developed with a powerful geometrical tool, the Poincaré map [20,45], obtained as the intersection of the phase space with a transversal surface, which eliminates one of the system dimensions. A fixed point of the map corresponds to a periodic solution of the system and a limit cycle of the map corresponds to a quasiperiodic solution [20,45]. Cartwright noted different qualitative behavior in regions near the codimension two bifurcation point: for some parameter values, the Poincaré map exhibits a limit cycle and fixed points, whereas for others it only exhibits fixed points. Therefore, additional bifurcation points must be present, giving rise to the onset of a limit cycle. The missing global bifurcation points are *saddle connections* [20]. At a *saddle connection* in the Poincaré map [45], the stable and

unstable manifolds of a saddle point intersect and forms a loop known as homoclinic orbit [20,45]. Further variation of the parameter destroys the homoclinic orbit generating a limit cycle (a quasiperiodic solution). The bifurcation can be visualized in the reverse sense: under the continuous variation of a parameter, the limit cycle collides with the saddle point and disappears, annihilating the quasiperiodic solution [20].

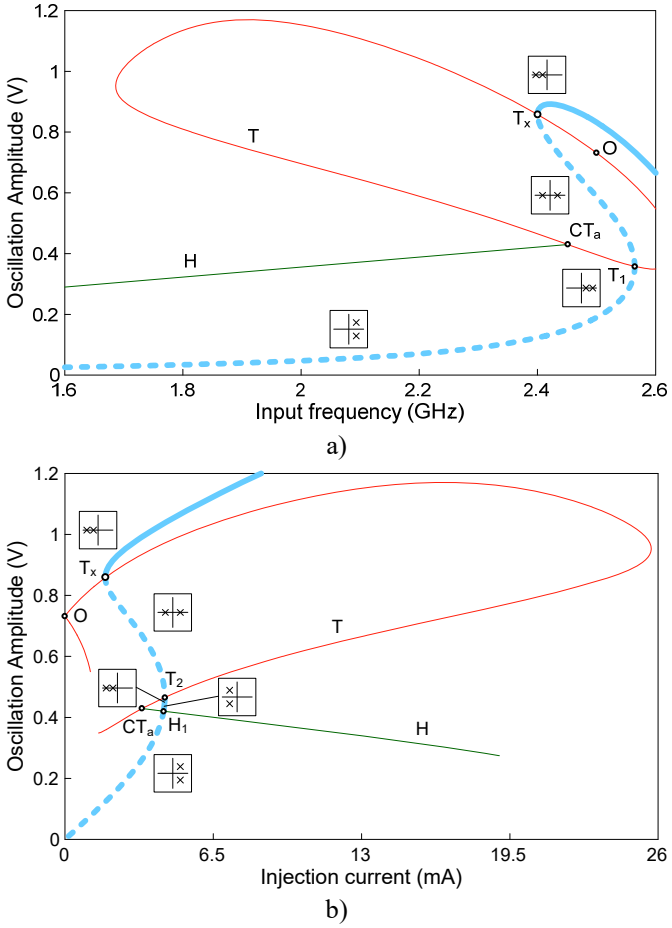

Fig. 10. Periodic solution curves of the ring oscillator in Fig. 3(a) passing through T_x. The evolution of the relevant poles along the periodic curve has been included in the insets. The unstable sections are traced in dashed line. The turning point and Hopf bifurcation loci are also superimposed. (a) Solution curve obtained for constant injection current $I_s = 1.772$ mA. (b) Solution curve obtained for constant input frequency $f_s = 2.4$ GHz. Note that the solutions of sections $T_x - T_1$ and $T_x - T_2$ are of saddle type [20,45].

The saddle connection bifurcation has hardly been investigated in the microwave literature [19]. In fact, obtaining the saddle-connection locus is not straightforward. Compared with a limit cycle generated/extinguished at a Hopf bifurcation, the limit cycle created/destructed at a saddle connection has non zero amplitude and frequency tending to zero, as the trajectories tend to spend long time near the saddle point. The existence of the saddle-connection locus in the ring oscillator of Fig. 3(a) will be analyzed next, combining the information provided by the bifurcation loci with the Poincaré map obtained from transient simulations.

B. Poincaré map from transient simulations

The Poincaré map (intersection of the phase space with a transversal surface) is relatively easy to compute for low-dimension systems using transient simulations. Using proper perturbations, it is able to detect even unstable solutions. For a better understanding of the evolution of the trajectories, the discrete set of points of the perturbed map will be connected with straight lines when representing the results. An optimum way of tracing a perturbed Poincaré map is to compute first a transient simulation from fixed initial conditions. This allows guessing the simulation time needed to reach the steady-state, starting always from the same initial conditions. Then, the steady state is perturbed at a fixed perturbation time t_p. In nonautonomous systems, such as injection-locked oscillators, the Poincaré map can be computed from t_p by sampling the state variables at integer multiples of the input generator period $T = 2\pi/\omega_s$. Note that starting the map computation at a different initial time means taking a different point of the periodic orbit with different values of the state variables, hence the importance of fixing the perturbation time. It is important to use a constant time step t_h in the integration method of the transient simulation. For convenience, an "oversample" value M for the time step $t_h = T/M$ is selected to ensure good convergence of the transient simulation. Then, the map is simply constructed by taking one point every M samples. The value $M = 32$ will be enough for most cases.

Here, the three-stage ring oscillator in Fig. 3(a) will be considered. This is an obvious choice for geometrical reasons: the phase space has dimension 3, providing a planar Poincaré map. In circuits containing lumped elements, the state variables preferred are usually voltages for capacitors and currents for inductors. The three state variables of the ring oscillator are the load voltages. The state variables chosen for the Poincaré map will be the two node voltages v_1, v_2 in Fig. 3(a). Note that introducing a perturbation of a state variable of the same kind, that is, perturbing a capacitor voltage with a voltage or an inductor current with a current, is not the best way, as it forces the circuit overall response rather than adding a perturbation. Therefore, the three node voltages will be perturbed with current sources. However, when proceeding like this, the starting point of the Poincaré map for a particular set of perturbations is not clearly identified. This is solved tracing what could be called "constellation of initial conditions", that is, the first point of the Poincaré map from a triple sweep of the three perturbation currents. Note that only the simulation time from t_p up to the first sample needs to be computed.

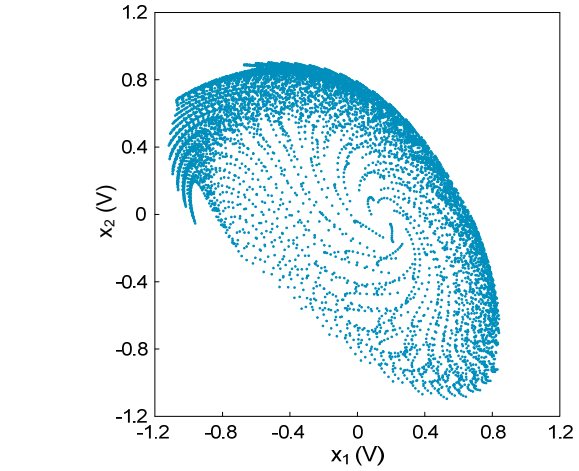

a)

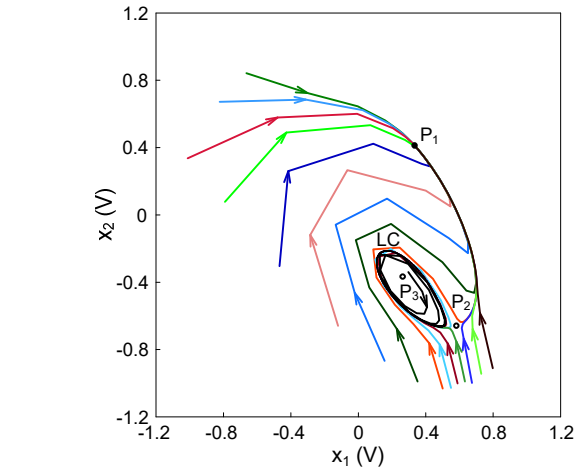

b)

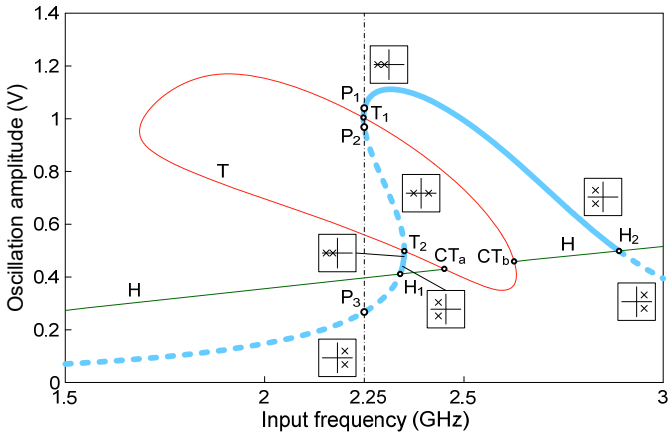

c)

Fig. 11. Coexisting solutions for $f_s = 2.25$ GHz and $I_s = 5.4$ mA in the ring oscillator of Fig. 3(a). (a) Constellation map of initial conditions obtained for $t_p = 10^4 t_h$. The three perturbing currents are swept from −200 mA up to 200 mA in steps of 20 mA. (b) Resulting Poincaré map traced from a subset of the previous initial conditions, carefully selected, delimiting four coexisting solutions: P_1, a sink, P_2, a saddle, P_3, an unstable focus and LC, a limit cycle. (c) The previous solutions over the curve obtained for $I_s = 5.4$ mA with the new frequency-domain techniques (unstable sections in dashed line). The turning point and Hopf loci are also superimposed.

The constellation map for the ring oscillator in Fig. 3(a) has been computed for the following parameter values: input frequency 2.25 GHz, injection current 5.4 mA and perturbation time $10^4 t_h$. The three perturbing currents are swept from −200 mA up to 200 mA in steps of 20 mA, providing the constellation map shown in Fig. 11(a). A subset of these initial conditions has been carefully selected to trace the Poincaré map shown in Fig. 11(b). Clearly, four different steady-state solutions can be identified [20,45]: three fixed points P_1, P_2 and P_3, and a limit cycle LC. This limit cycle is composed of nonconsecutive discrete points due to the nonrational relationship between the frequencies (rotation number). The limit cycle will be eventually filled as time tends to infinity [20,45]. The fixed point P_1 is a stable node (a sink), P_2 is a saddle, P_3 is an unstable focus and LC is a stable limit cycle. These solutions are in agreement with the results obtained with the new frequency-domain methodology [Fig. 11(c)]: indeed, the isoline corresponding to $I_s = 5.4$ mA is three times intersected by the vertical line corresponding to $f_s = 2.25$ GHz. The solution with largest amplitude is the sink P_1, the solution between T_1 and T_2 is the saddle P_2 and the low-amplitude solution is the unstable focus P_3. On the other hand, the limit cycle LC observed in the Poincaré map corresponds to a quasiperiodic solution generated at H_1 in Fig. 11(c) when reducing the input frequency. Note that the points of the limit cycle are not connected with straight lines so that the Poincaré map does not get smudged.

C. *Saddle-connection locus*

Saddle connection bifurcations have been investigated with the Poincaré map. The analyses in Fig. 12 have been carried out for an input frequency value $f_s = 2.25$ GHz. In Fig. 12(a) for $I_s = 5.1$ mA, a saddle is observed very close to a limit cycle. In Fig. 12(b) for slightly lower injection current $I_s = 5$ mA, the limit cycle is suddenly destroyed. This is due to a collision between the limit cycle and the saddle giving rise to a saddle connection bifurcation. To obtain the saddle-connection locus, the analysis is repeated for different input frequency values, which provides the locus represented in Fig. 12(c). The saddle-connection, turning point and Hopf bifurcation loci meet at the codimension two bifurcation point CT_a. Indeed, the Center Manifold Theorem [20-21,47-48] provides, under some non-degeneracy conditions, an analytical normal form for an *n*-dimensional system that is topologically equivalent near CT_a [20]. This normal form provides an interesting geometrical result: the three bifurcation loci meeting at the codimension two bifurcation are tangent to each other. Fig. 12(c) evidences this result.

The saddle-connection locus meets the turning point locus at a second point *S* in Fig. 12(c). The study of the Poincaré map reveals that turning points on the right of *S* are synchronization points, whereas the turning points on the left

are jump points. An important conclusion is derived: the point *S* acts as a separator between synchronization points and jump points. An identical study has been carried out for a Van der Pol oscillator, obtaining the same conclusion. At a synchronization point, like T_x in Fig. 10, a saddle and a node of the Poincaré map are connected by the unstable manifold of the saddle, forming a homoclinic orbit [20-21]. After the bifurcation (desynchronization), this orbit becomes a limit cycle (quasiperiodic solution). It is therefore quite easy to distinguish between jump points and synchronization points in the Poincaré map. In the case of jump points, the limit cycle already exists and the collision between the saddle and the node occurs outside the limit cycle. In the case of synchronization points, the limit cycle is created after the collision between the saddle and the node in the homoclinic orbit.

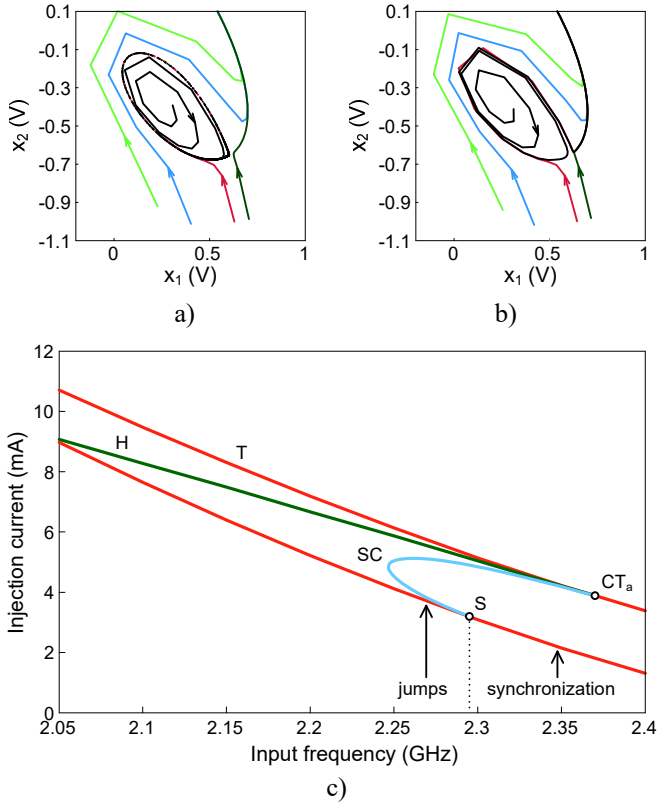

Fig. 12. Detection of saddle connections in the ring oscillator of Fig. 3(a) by means of the Poincaré map. (a) A region of the Poincaré map traced for $I_s = 5.1$ mA and $f_s = 2.25$ GHz showing a saddle very close to a limit cycle. (b) The same region traced for $I_s = 5$ mA. The limit cycle has been destroyed due to a collision with the saddle. (c) Bifurcation loci in the neighborhood of the saddle-connection locus obtained from direct observation of the bifurcations in the Poincaré map.

Saddle connections are susceptible to give rise to homoclinic chaos. This chaotic behavior will be demonstrated next using envelope transient simulations.

D. Detection of homoclinic chaos with envelope transient

Saddle connections in the Poincaré map imply the formation of homoclinic orbits, leading to complicated dynamics: iterations of the map with transverse homoclinicity have been demonstrated to provide a horseshoe map [20,46,48], or equivalently, chaotic dynamics. Therefore, homoclinic chaos will be observed in the neighborhood of the saddle-connection points. Note that the qualitative dynamics discussed in this section are general to any injection-locked oscillator, so these circuits will exhibit homoclinic chaos for certain values of input power and frequency. The size of the chaotic region will vary from circuit to circuit.

Despite the limitations of envelope transient when dealing with broadband signals, this method has enabled the detection of chaotic solutions of the ring oscillator in Fig. 3(a). The point $f_s = 2.26$ GHz, $I_s = 4.11$ mA, belonging to the saddle-connection locus in Fig. 12(c), is selected. An AG with amplitude $V_{AG} = 0.1985$ V and phase $\phi_{AG} = 100.1$ deg is connected the first 11 ns to excite the desired solution and then it is disconnected. The envelope simulation time is 40 us with a time step of 0.14 ns and an initial offset of 800 ns. The results are displayed in Fig. 13. The irregular behavior, shown in Fig. 13(a), is characteristic of chaos. The continuous spectrum, shown in Fig. 13(b), observed is also characteristic of chaotic behavior.

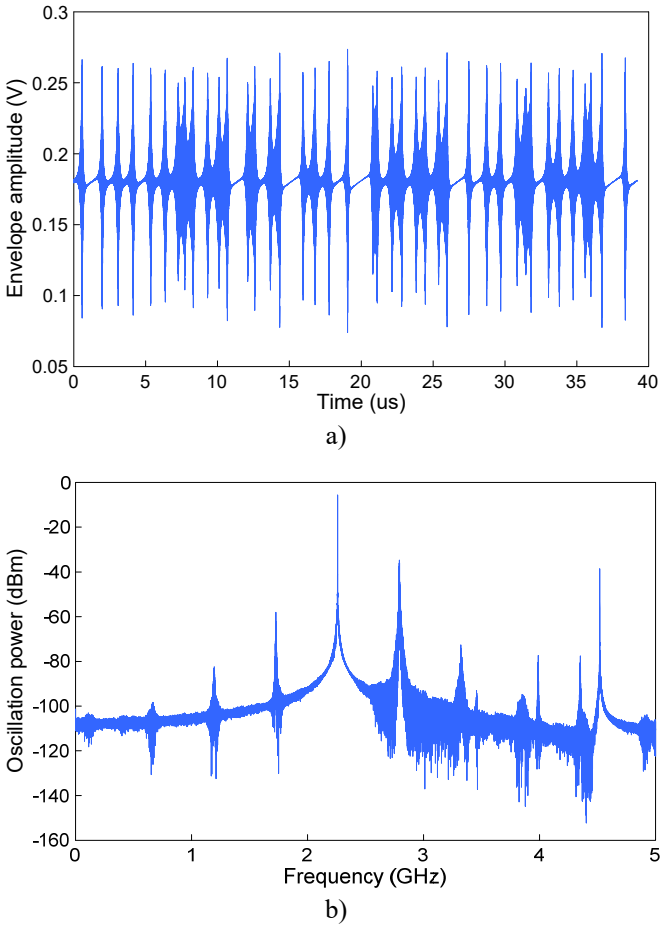

Fig. 13. Detection of homoclinic chaos near the saddle-connection locus of Fig. 12(c) by means of envelope transient simulations. (a) Chaotic envelope. (b) Chaotic spectrum (continuous spectrum) computed from the waveform.

VI. Application to an Experimental Oscillator

The methodology presented will be applied to the prototype presented in [49-50]. The experimental circuit in Fig. 14(a) is a single-ended three-stage ring oscillator based on NE3210S01 FET built on RO4003 substrate (h = 0.508 mm, $\varepsilon_r = 3.38$). Full models have been considered for the transistor devices, including all the parasitics. This particular circuit constitutes a challenging demonstrator of the capabilities of the new simulation method, due to the complexity of its synchronized solution curves. The oscillator exhibits multimode behavior, that is, stable oscillations with different frequencies and amplitudes coexist for particular parameter values. However, a thorough observation of the free-running bifurcation diagram versus the gate bias voltage (V_{GS}) in Fig. 14(d) reveals that monomode behavior, as in any well-behaved oscillator, can be obtained in a certain interval of V_{GS}. Indeed, only the mode 4 at 12.9 GHz is obtained in the gate bias voltage interval $[-1.71, -1.53]$ V. This oscillation mode arises from a subcritical Hopf bifurcation from dc regime [39-40,49], and two different steady-state free-running oscillations coexist in the interval indicated. The two solutions correspond to the same mode (same solution curve), although only the one with highest amplitude is stable. When connecting an injection source to the oscillator and increasing the input power level, synchronization curves will arise around both the stable and unstable free-running oscillations. Indeed, both solutions synchronize with the input source, despite their stability properties. When tracing the injection-locked solution curves versus the input frequency, for low input power, two different sets of closed curves will be obtained. Because the amplitudes and frequencies of the free-running solutions are relatively close, the synchronized solution curves of each solution are likely to merge and provide a single closed curve for certain input power. When further increasing the input power, this closed curve will also merge with the coexisting low-amplitude solution, as already discussed in Section III.

None of the load nodes V_1, V_2, V_3 indicated in Fig. 14(b) have been found to be sensitive enough to excite the circuit oscillation. Therefore, it is necessary to use the methodology described in Section II-C. The microstrip "tee" interconnecting each 50-Ohm load with the ring core is modeled with three microstrip lines connected in T, as shown in Fig. 14(b). This model is found accurate enough since no significant change is observed in the free-running bifurcation diagram of Fig. 14(d) when using the T model extracted from electromagnetic simulations of the structure. Inside the equivalent T, a sensitive internal node V_i, shown in Fig. 14(b), is available for the application of the generalized outer-tier contour method presented in Section II-C. The input linear network, as gathered from Fig. 14(b), is constituted by the 50-Ohm load and the microstrip line TL_1. The output power at the node V_1 [where the spectrum analyzer is connected in Fig. 14(c)] is calculated providing the results obtained with the outer-tier contour to an AG connected to the node V_i. The output power curves are presented in Fig. 15(a), obtained for input power values from −20 dBm up to 10 dBm in steps of 5 dB. The results are validated with standard optimization and parameter switching, showing excellent agreement. Tracing the complicated geometries of the solution curves applying parameter switching with no previous knowledge of the turning points is highly involved and time-consuming. On the contrary, obtaining the solution curves with the outer-tier contour method is straightforward.

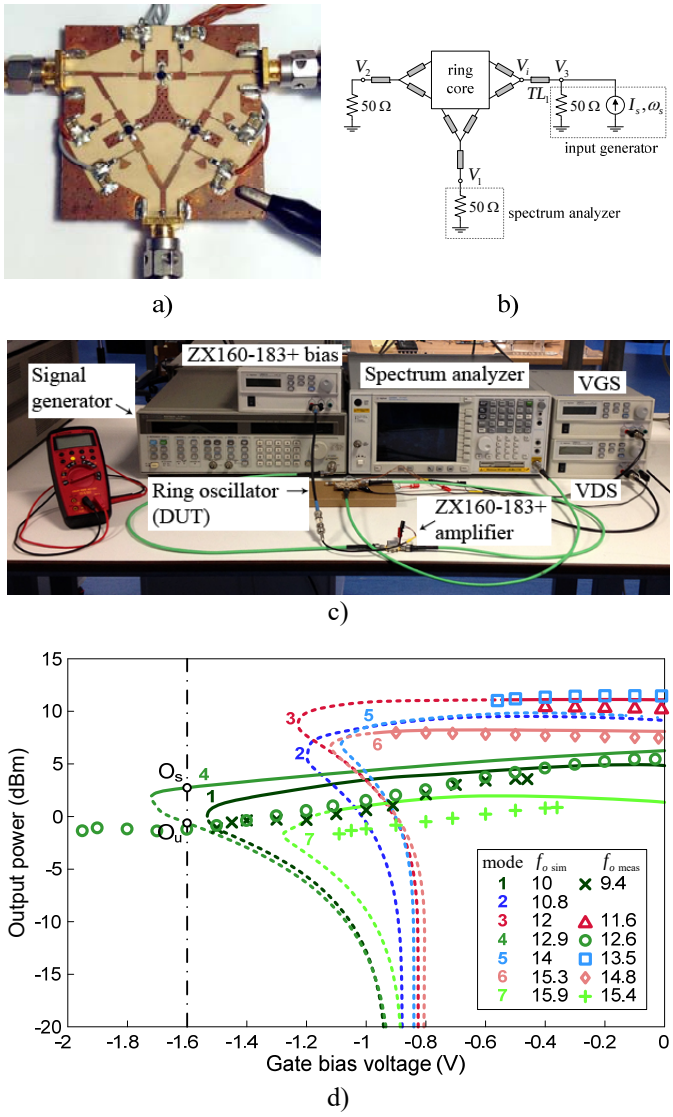

Fig. 14. (a) Photograph of the single-ended three-stage ring oscillator based on NE3210S01 FET. (b) Schematic of the oscillator including an approximate model of the interconnection "tees". (c) Photograph of the measurement setup. (d) Free-running oscillation modes: output power at the first harmonic versus gate bias voltage. Unstable sections are traced in dashed line. Measurements (symbols) are superimposed.

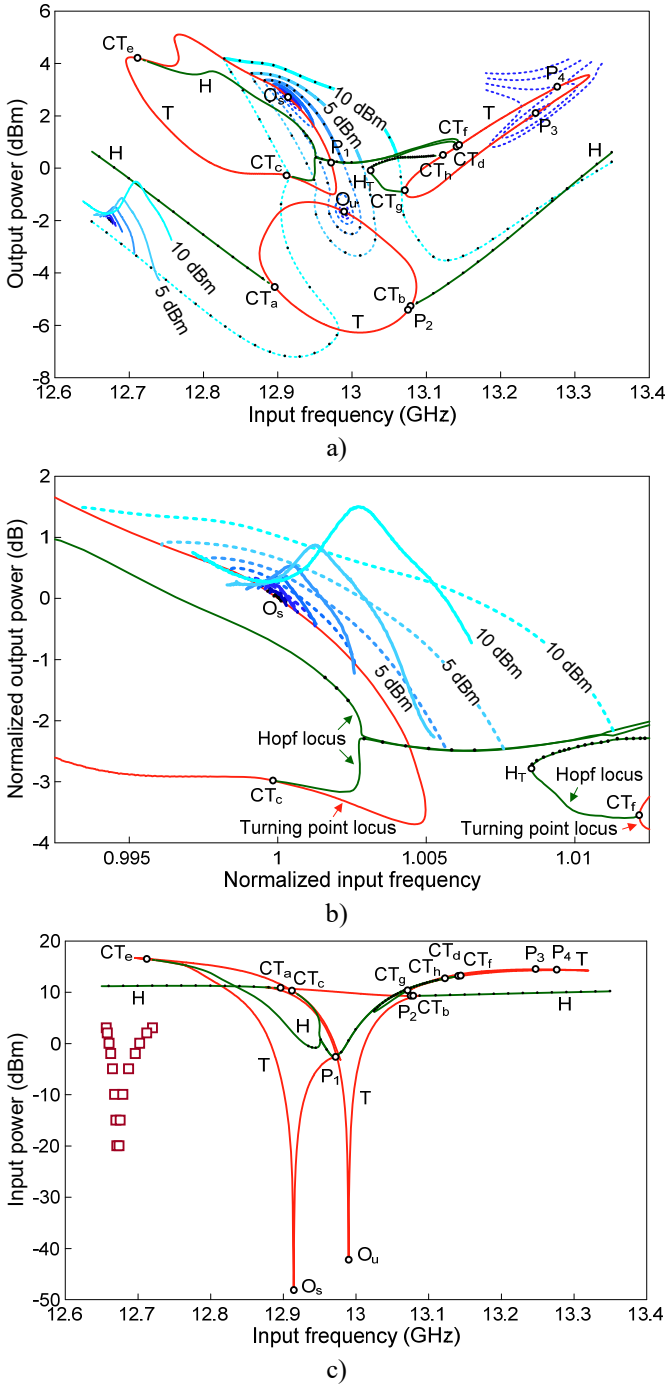

Fig. 15. (a) Periodic solution curves (output power versus input frequency) and bifurcation loci of the experimental ring oscillator. Both the periodic solution curves and Hopf bifurcation locus are compared with the results of the previous AG-based techniques, represented with dots. The stable (unstable) sections of the solution curves are in solid (dashed) line. In all cases the HB system has been solved using $NH = 15$ harmonic terms. The set of synchronization curves around 12.67 GHz are the ones measured. (b) Expanded view of the measurements (solid line) and simulated results (dashed line), where the amplitudes and frequencies have been normalized to the free-running ones, respectively. Note the points of the Hopf bifurcation locus (dots) obtained with the previous AG-based technique. (c) Input power versus input frequency. Measurements (square symbols) match the results obtained in simulation with a slight frequency and amplitude offset.

The free-running oscillation points O_s and O_u corresponding to the stable and the unstable solutions, respectively, are in agreement with the results already obtained in the free-running bifurcation diagram of Fig. 14(d). The oscillation power and frequency of the stable solution are respectively 2.7 dBm and 12.91 GHz. The oscillation power and frequency of the unstable solution are respectively −1.7 dBm and 12.99 GHz. When increasing the input power, two sets of closed curves are obtained, which, in agreement with previous discussions, merge at point P_1 (corresponding to an input power of −2.6 dBm). When further increasing the input power [Fig. 14(d)], a single set of closed solution curves is obtained, which merges with the low amplitude curve at P_2 (corresponding to an input power of 9.3 dBm). Additional solution curves, corresponding to injection current values $I_s = 65$ mA, 66 mA, 67 mA and 68 mA, are included in Fig. 15(a) to illustrate the behavior around the merging points P_3 and P_4. All these sections are unstable, as verified with pole-zero identification [44].

The turning point and Hopf bifurcation loci, together with the codimension two bifurcations, have been superimposed in Fig. 15(a). The intricate multivalued Hopf bifurcation locus could only be completed with the new method, based on condition (20). The points obtained with the former method [16], based on solving (19), are overlapped [see also Fig. 15(b)]. However, convergence could only be obtained in rather small sections of the Hopf bifurcation locus, as shown in the figure (superimposed dots): it was not possible to detect the lower section of this locus since a discontinuous jump was observed between two different sections at the infinite slope point H_T [see Fig. 15(a), 15(b)]. The new zero-level contour technique predicts these sections and evidences the presence of H_T. For illustration, Fig. 16(a) presents the contour curves $\mathrm{Re}[Y_a] = 0$ and $\mathrm{Im}[Y_a] = 0$ obtained at the particular injection frequency $f_s = 13.055$ GHz. The intersections predict four Hopf bifurcations in agreement with the bifurcation diagram in Fig. 15(a). The validity of (20) has been verified with an independent stability analysis based on pole-zero identification [44]. This analysis has been performed at a constant input power of 10 dBm. The results are shown in Fig. 16(b), where the real parts of two different pairs of complex-conjugate poles are traced versus the input frequency (the imaginary part of each pair is respectively 13.156 GHz and 12.942 GHz at $f_s = 13.05$ GHz). The four zero crossings H_1, H_2, H_3, H_4 are in total agreement with the four intersections of the solution curve corresponding to 10 dBm with the multivalued Hopf bifurcation locus in Fig. 15(a).

The stable and unstable sections of the periodic solution curves in Fig. 15(a) (verified with pole-zero identification [44]) are traced with solid line and dashed line, respectively. Measured results are also superimposed in Fig. 15(a). Note that comparisons can only be performed between stable sections of the curves and measurements, since unstable sections are unphysical. There is a small offset in frequency and power attributed to modeling inaccuracies in the hybrid prototype and the transistor biasing below threshold voltage.

An expanded view of the curves normalized to the free-running amplitudes and frequencies is also presented in Fig. 15(b) for a detailed comparison. Up to −5 dBm, measurements should be compared with the closed synchronization curves about O_s. In that power range, the synchronization bandwidth is delimited, for each power value, by the turning points of the corresponding closed synchronization curve. These are synchronization points (local-global bifurcations) instead of hysteresis points, in consistency with the absence of any stable periodic solution prior to the turning point on the left and after the turning point on the right. For input power 0 dBm, 5 dBm and 10 dBm, the experimental bandwidth agrees approximately with that of the stable section of the periodic solution curve obtained in simulation. This stable section is limited on the left side (lower input frequency) by a local-global turning point bifurcation, associated with synchronization/desynchronization. On the right side (higher input frequency), it is limited by a Hopf bifurcation, as shown in Fig. 15(a), 15(b).

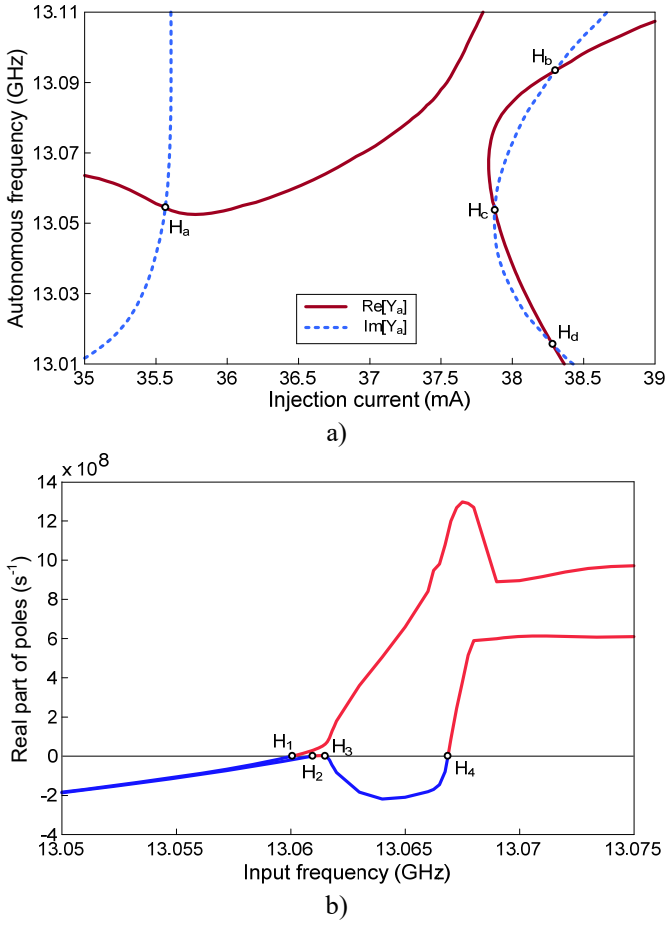

Fig. 16. Multivalued Hopf bifurcation locus. (a) Contour curves $\mathrm{Re}[Y_a]=0$ and $\mathrm{Im}[Y_a]=0$ obtained at the particular injection frequency $f_s=13.055$ GHz. (b) Pole-zero identification of the solution curve corresponding to an input power of 10 dBm. The real part of the poles is traced versus the input frequency. The four zero crossings validate the four intersections of the solution curve 10 dBm with the Hopf bifurcation locus in Fig. 15(a).

The bifurcation loci have also been represented in the plane defined by the input frequency and the input power (in dBm), providing two V-shaped synchronization regions [16,23] shown in Fig. 15(c). Only the one on the left-hand side corresponds to physical solutions. The measurements (square symbols) are included in Fig. 15(c) and show good agreement with the turning point locus on the left-hand side. Again, a small offset in input frequency and power is observed due to modeling inaccuracies. To summarize, the major discrepancy comes from the free-running oscillation frequency which is 240 MHz smaller in measurements and represents an error of 1.9%. Because the bandwidth (reasonable well predicted in the simulations) is relatively small, simulation and measurements cannot overlap, as in case of [43].

Finally, chaos is measured for an input power value of 12 dBm in agreement with the discussion in Section V-D. Measurements in Fig. 17 show chaotic behavior when increasing the input frequency. The chaotic spectrum arises suddenly, with no intermediate observation of quasiperiodic solution, either when increasing or decreasing the input frequency. This fact strongly suggests homoclinic chaos. For $f_s=12.77$ GHz, the periodic injection-locked oscillation is observed in Fig. 17(a). Then, for f_s between 12.771 GHz and 12.773 GHz, a spectral regrowth appears in Figs. 17(b-d) about the spectral line corresponding to the input frequency. The resolution bandwidth of the spectrum analyzer is lowered to 51 kHz to highlight it is a continuous spectrum, which is characteristic of chaotic behavior. Finally, Fig. 17(e), corresponding to $f_s=12.774$ GHz, shows a discrete spectrum composed of individual spectral lines, with no region with continuous spectrum. This quasiperiodic solution implies the transition from chaos to the mixer-like regime where the input signal mixes with the autonomous oscillation of the circuit.

VII. Conclusion

A new methodology has been presented for the efficient harmonic balance analysis of injection-locked oscillators, exhibiting complex multivalued solution curves in the low and intermediate input power ranges. Unlike previous analysis techniques, it does not require any optimization or parameter switching procedures. In combination with additional mathematical conditions, it enables a straightforward determination of the turning point and Hopf bifurcation loci that delimit the stable synchronization bands, often exhibiting intricate geometries. The codimension two bifurcation where the turning point and Hopf bifurcation loci merge has been investigated in detail, as well as the saddle-connection locus, analyzed in microwave circuits for the first time to our knowledge. The likely observation of chaos near the codimension two bifurcation has been discussed. The techniques have been applied to several injection-locked oscillators, obtaining good agreement between results and measurements.

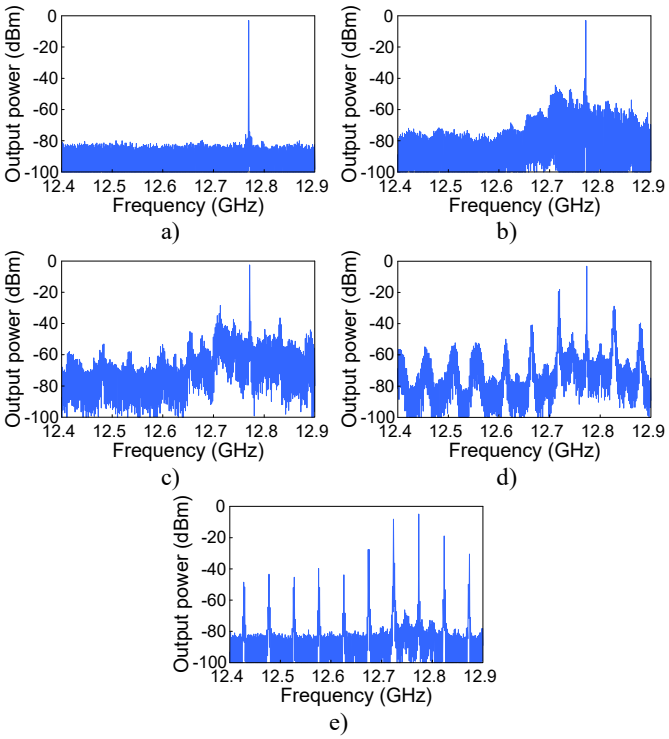

Fig. 17. Measured spectrum for $P_s = 12$ dBm in the experimental ring oscillator of Fig. 14(a). (a) Periodic spectrum obtained for $f_s = 12.77$ GHz. (b)-(d) Continuous spectra obtained for $f_s = 12.771$ GHz, 12.772 GHz, 12.773 GHz, respectively, evidencing chaotic behavior. (e) Quasiperiodic spectrum obtained for $f_s = 12.774$ GHz.

REFERENCES

[1] B. Razavi, "A study of injection locking and pulling in oscillators," *IEEE J. Solid-State Circuits*, vol. 39, no. 9, pp. 1415–1424, Sept. 2004.

[2] A. Mazzanti and F. Svelto, "A 1.8-GHz injection-locked quadrature CMOS VCO with low phase noise and high phase accuracy," *IEEE Trans. Circuits Syst. I, Reg. Papers*, vol. 53, no. 3, pp. 554–560, Mar. 2006.

[3] M.K. Kazimierczuk, V.G. Krizhanovski, J.V. Rassokhina, and D.V. Chernov, "Injection-locked class-E oscillator," *IEEE Trans. Circuits Syst. I, Reg. Papers*, vol. 53, no. 6, pp. 1214–1222, Jun. 2006.

[4] C.-T. Chen, T.-S. Horng, K.-C. Peng, and C.-J. Li, "High-Gain and High-Efficiency EER/Polar Transmitters Using Injection-Locked Oscillators," *IEEE Trans. Microw. Theory Techn.*, vol. 60, no. 12, pp. 4117–4128, Dec. 2012.

[5] E.F. Calandra, D. Lupo, and L. Puccio, "A DRO-based X-band injection-locked amplifier without input non-reciprocal elements," in *Europ. Conf. Circuit Theory and Design*, 2009, pp. 367–370.

[6] H. Cho, J. Bae, and H.-J. Yoo, "A 39 μW body channel communication wake-up receiver with injection-locking ring-oscillator for wireless body area network," in *IEEE Int. Symp. on Circuits and Syst.*, 2012, pp. 2641–2644.

[7] B. N. Biswas, A. Bhattacharya, P. Lahiri, and D. Mondal, "A novel scheme for reception using an active microstrip antenna," *IEEE Trans. Microw. Theory Techn.*, vol. 48, no. 10, pp. 1765–1768, Oct. 2000.

[8] E. Main and D. Coffing, "An FSK demodulator for Bluetooth applications having no external components," *IEEE Trans. Circ. Syst. II*, vol. 49, no. 6, pp. 373–378, Jun. 2002.

[9] V.F. Fusco, "Polarisation-diversity phase-encoded patch-antenna transponder," *IEE Proc. Microw. Antennas Propagat*, vol. 144, no. 3, pp. 201–204, Jun. 1997.

[10] H. Grubinger, G. von Buren, H. Barth, and R. Vahldieck, "Continuous Tunable Phase Shifter Based on Injection Locked Local Oscillators at 30 GHz," *IEEE MTT-S Int. Microwave Symp. Dig.*, 2006, pp. 1821–1824.

[11] W.-J. Tseng, Z.-M. Tsai, C.-S. Lin, and H. Wang, "Ku-band phase shifter based on injection locked voltage oscillator," in *IEEE Int. Conf. on Wireless Inform. Technol. and Syst.*, 2010, pp. 1–4.

[12] S. Patnaik and R. Harjani, "A 24-GHz phased-array receiver in 0.13-μm CMOS using an 8-GHz LO," in *IEEE Radio Freq. Integr. Circuits Symp.*, 2010, pp. 465–468.

[13] V. Rizzoli and A. Neri, "State of the art and present trends in nonlinear microwave CAD techniques," *IEEE Trans. Microw. Theory Techn.*, vol. 36, no. 2, pp. 343–365, Feb. 1988.

[14] R. Quéré, E. Ngoya, M. Camiade, A. Suárez, M. Hessane, and J. Obregón, "Large signal design of broadband monolithic microwave frequency dividers and phase-locked oscillators," *IEEE Trans. Microw. Theory Techn.*, vol. 41, no. 11, pp. 1928–1938, Nov. 1993.

[15] A. Suárez and R. Quéré, *Stability Analysis of Nonlinear Microwave Circuits*. Boston, MA: Artech House, 2003.

[16] A. Suárez, *Analysis and Design of Autonomous Microwave Circuits*. Hoboken, New Jersey: John Wiley & Sons, 2009.

[17] G.H.B. Hansson and K.I. Lundstrom, "Stability Criteria for Phase-Locked Oscillators," *IEEE Trans. Microw. Theory Techn.*, vol. 20, no. 10, pp. 641–645, Oct. 1972.

[18] E.F. Calandra and A.M. Sommariva, "Stability Analysis of Injection-Locked Oscillators in Their Fundamental Mode of Operation," *IEEE Trans. Microw. Theory Techn.*, vol. 29, no. 11, pp. 1137–1144, Nov. 1981.

[19] A. Suárez, J. Morales, and R. Quéré, "Synchronization analysis of autonomous microwave circuits using new global-stability analysis tools," *IEEE Trans. Microw. Theory Techn.*, vol. 46, no. 5, pp. 494–504, May 1998.

[20] J. Guckenheimer and P. Holmes, *Nonlinear Oscillations, Dynamic Systems, and Bifurcations of Vector Fields*. New York: Springer-Verlag, 1983.

[21] J. M. T. Thompson and H. B. Steward, *Nonlinear Dynamics and Chaos*. Chichester: Wiley, 1986.

[22] F. Ramírez, M. Pontón, S. Sancho, and A. Suárez, "Phase-Noise Analysis of Injection-Locked Oscillators and Analog Frequency Dividers," *IEEE Trans. Microw. Theory Techn.*, vol. 56, no. 2, pp. 393–407, Feb. 2008

[23] F. Ramírez, M.E. de Cos, and A. Suárez, "Nonlinear analysis tools for the optimized design of harmonic-injection dividers," *IEEE Trans. Microw. Theory Techn.*, vol. 51, no. 6, pp. 1752–1762, Jun. 2003.

[24] E. Palazuelos, A. Suárez, J. Portilla, and F.J. Barahona, "Hysteresis prediction in autonomous microwave circuits using commercial software: application to a Ku-band MMIC VCO," *IEEE J. Solid-State Circuits*, vol. 33, no. 8, pp. 1239–1243, Aug. 1998.

[25] S. Jeon, A. Suárez, and D.B. Rutledge, "Analysis and elimination of hysteresis and noisy precursors in power amplifiers," *IEEE Trans. Microw. Theory Techn.*, vol. 54, no. 3, pp. 1096–1106, Mar. 2006.

[26] S. Jeon, A. Suárez, and D.B. Rutledge, "Global stability analysis and stabilization of a class-E/F amplifier with a distributed active transformer," *IEEE Trans. Microw. Theory Techn.*, vol. 53, no. 12, pp. 3712–3722, Dec. 2005.

[27] N. Ayllon, J.M. Collantes, A. Anakabe, I. Lizarraga, G. Soubercaze-Pun, and S. Forestier, "Systematic Approach to the Stabilization of Multitransistor Circuits," *IEEE Trans. Microw. Theory Techn.*, vol. 59, no. 8, pp. 2073–2082, Aug. 2011.

[28] N. Ayllon, A. Anakabe, J.-M. Collantes, G. Soubercaze-Pun, and S. Forestier, "Sensitivity enhancement in pole-zero identification based stability analysis of microwave circuits," in *Workshop on Integr. Nonlinear Microw. and Millimetre-Wave Circuits*, 2008, pp. 75–78.

[29] I. Angelov, H. Zirath, and N. Rorsman, "A new empirical nonlinear model for HEMT and MESFET devices," *IEEE Trans. Microw. Theory Techn.*, vol. 40, no. 12, pp. 2258–2266, Dec. 1992.

[30] A. Gelb and W. E. Vander Velde, *Multiple-input describing functions and nonlinear system design*. New York: McGraw-Hill, 1968.

[31] R.C. Melville, P. Feldmann, and J. Roychowdhury, "Efficient multi-tone distortion analysis of analog integrated circuits," in *Proc. IEEE Custom Integr. Circuits Conf.*, 1995, pp. 241–244.

[32] V. Rizzoli, A. Lipparini, D. Masotti, and F. Mastri, "Efficient circuit-level analysis of large microwave systems by Krylov-subspace harmonic balance," *IEEE MTT-S Int. Microwave Symp. Dig.*, 2001, pp. 25–28.

[33] V. Rizzoli, F. Mastri, C. Cecchetti, and F. Sgallari, "Fast and robust inexact Newton approach to the harmonic-balance analysis of nonlinear

microwave circuits," *IEEE Microwave Guided Wave Lett.*, vol. 7, no. 10, pp. 359–361, Oct. 1997.
[34] A. Gray, *Modern Differential Geometry of Curves and Surfaces with Mathematica, 2nd ed*. Boca Raton: CRC Press, 1997.
[35] S. Wiggins, *Introduction to Applied Nonlinear Dynamical Systems and Chaos*. New York: Springer-Verlag, 1990.
[36] G. Iooss and D. D. Joseph, *Elementary Stability and Bifurcation Theory*. New York: Springer-Verlag, 1997.
[37] F.-H. Huang and Y.-J. Chan, "A V-Band CMOS Injection-Locked Oscillator Using Fundamental Harmonic Injection," *IEEE Microw. Wireless Compon. Lett.*, vol. 17, no. 12, pp. 882–884, Dec. 2007.
[38] S. Lee, S. Jang, and C. Nguyen, "Low-Power-Consumption Wide-Locking-Range Dual-Injection-Locked 1/2 Divider Through Simultaneous Optimization of VCO Loaded Q and Current," *IEEE Trans. Microw. Theory Techn.*, vol. 60, no. 10, pp. 3161–3168, Oct. 2012.
[39] J. Marsden and M. McCracken, *Hopf Bifurcation and Its Applications*. New York: Springer-Verlag, 1976.
[40] N. V. Butenin, Y. I. Neimark, and N. A. Fufaev, *An Introduction to the Theory of Nonlinear Oscillations*. Moscow, Russia: Mir Publishers, 1987.
[41] J. M. Paillot, J. C. Nallatamby, M. Hessane, R. Quéré, M. Prigent, and J. Rousset, "A general program for steady state, stability, and FM noise analysis of microwave oscillators," *IEEE MTT-S Int. Microwave Symp. Dig.*, 1990, pp. 1287–1290.
[42] V. Rizzoli, F. Mastri, and D. Masotti, "General noise analysis of nonlinear microwave circuits by the piecewise harmonic-balance technique," *IEEE Trans. Microw. Theory Techn.*, vol. 42, no. 5, pp. 807–819, May 1994.
[43] A. Collado and A. Suárez, "Application of bifurcation control to practical circuit design," *IEEE Trans. Microw. Theory Techn.*, vol. 53, no. 9, pp. 2777–2788, Sept. 2005.
[44] J. Jugo, J. Portilla, A. Anakabe, A. Suárez, and J. M. Collantes, "Closed-loop stability analysis of microwave amplifiers," *Electron. Lett.*, vol. 37, no. 4, pp. 226–228, Mar. 2001.
[45] T. S. Parker and L. O. Chua, *Practical Numerical Algorithms for Chaotic Systems*. New York: Springer-Verlag, 1989.
[46] C. P. Silva, "Shil'nikov's theorem-a tutorial," *IEEE Trans. Circuits Syst. I, Fundam. Theory Appl.*, vol. 40, no. 10, pp. 675–682, Oct. 1993.
[47] J. Carr, *Application of the Centre Manifold Theory, volume 35 of Applied Mathematical Sciences*. New York: Springer-Verlag, 1981.
[48] S. Smale, "Differentiable dynamical systems," *Bull. Amer. Math. Soc.* 73, pp. 747–817, 1967.
[49] J. de Cos, A. Suárez, and F. Ramírez, "Analysis of oscillation modes in free-running ring oscillators," *IEEE Trans. Microw. Theory Techn.*, vol. 60, no. 10, pp. 3137–3150, Oct. 2012.
[50] J. de Cos and A. Suárez, "Stability Analysis of Injection-Locked Multimode Oscillators," *IEEE Trans. Microw. Theory Techn.*, vol. 61, no. 8, pp. 2878–2891, Aug. 2013.

Jesús de Cos was born in Santander, Spain. He received the Telecommunications Engineering degree and the MSc degree from the University of Cantabria, Santander, Spain, in 2010 and 2011, respectively. He is currently working towards his Ph.D. degree at the University of Cantabria.

His research interests include stability analysis and bifurcation theory applied to analysis and design of microwave circuits.

Almudena Suárez (M'96–SM'01–F'12) was born in Santander, Spain. She received the Electronic Physics degree and Ph.D. degree from the University of Cantabria, Santander, Spain, in 1987 and 1992, respectively, and the Ph.D. degree in electronics from the University of Limoges, Limoges, France, in 1993.

She is currently a Full Professor with the University of Cantabria, where she is a member of the Communications Engineering Department. She authored *Analysis and Design of Autonomous Microwave Circuits* (IEEE, 2009) and coauthored *Stability Analysis of Nonlinear Microwave Circuits* (Artech House, 2003).

Dr. Suárez belongs to the Technical Committees of the IEEE International Microwave Symposium and European Microwave Conference. She was an IEEE Distinguished Microwave Lecturer (2006–2008). She is a member of the Board of Directors, European Microwave Association (EuMA). She is the editor-in-chief of the *International Journal of Microwave and Wireless Technologies* (Cambridge University Press).